AGU PUBLICATIONS

JGR

Journal of Geophysical Research: Oceans

RESEARCH ARTICLE

10.1002/2017JC013080

Fine-scale variability of isopycnal salinity in the California Current System

Sachihiko Itoh[1] and **Daniel L. Rudnick**[2]

[1]Atmosphere and Ocean Research Institute, The University of Tokyo, Kashiwa, Chiba, Japan, [2]Scripps Institution of Oceanography, La Jolla, California, USA

Key Points:
- Fine-scale isopycnal salinity variance is seasonally enhanced in frontal areas when the California Under Current is enhanced
- Spectral slope of the isopycnal salinity gradient with respect to wavenumber was 0.19 ± 0.27 over 12–60 km and -0.025 ± 0.32 over 12–30 km
- Variance increased with the steepening of the spectral slope in areas where the currents interacted with the topography

Correspondence to:
Sachihiko Itoh,
itohsach@aori.u-tokyo.ac.jp

Citation:
Itoh, S. and D. L. Rudnick (2017), Fine-scale variability of isopycnal salinity in the California Current System, *J. Geophys. Res. Oceans*, *122*, 7066–7081, doi:10.1002/2017JC013080.

Received 10 MAY 2017
Accepted 9 AUG 2017
Accepted article online 25 AUG 2017
Published online 1 SEP 2017

Abstract This paper examines the fine-scale structure and seasonal fluctuations of the isopycnal salinity of the California Current System from 2007 to 2013 using temperature and salinity profiles obtained from a series of underwater glider surveys. The seasonal mean distributions of the spectral power of the isopycnal salinity gradient averaged over submesoscale (12–30 km) and mesoscale (30–60 km) ranges along three survey lines off Monterey Bay, Point Conception, and Dana Point were obtained from 298 transects. The mesoscale and submesoscale variance increased as coastal upwelling caused the isopycnal salinity gradient to steepen. Areas of elevated variance were clearly observed around the salinity front during the summer then spread offshore through the fall and winter. The high fine-scale variances were observed typically above 25.8 kg m^{-3} and decreased with depth to a minimum at around 26.3 kg m^{-3}. The mean spectral slope of the isopycnal salinity gradient with respect to wavenumber was 0.19 ± 0.27 over the horizontal scale of 12–60 km, and 31%–35% of the spectra had significantly positive slopes. In contrast, the spectral slope over 12–30 km was mostly flat, with mean values of -0.025 ± 0.32. An increase in submesoscale variability accompanying the steepening of the spectral slope was often observed in inshore areas; e.g., off Monterey Bay in winter, where a sharp front developed between the California Current and the California Under Current, and the lower layers of the Southern California Bight, where vigorous interaction between a synoptic current and bottom topography is to be expected.

1. Introduction

The California Current System (CCS) is a confluence of the various water masses that make up the eastern North Pacific [*Reid and Schwartzlose*, 1962; *Lynn and Simpson*, 1987; *Rudnick et al.*, 2017]. The California Current (CC), an eastern boundary current of the subtropical gyre, transports cold fresh water from high-latitude regions equatorward, while the California Under Current (CUC), which flows poleward over the continental slope, carries warm saline water that originates from low latitude regions. The Inshore Countercurrent is a narrow poleward flow in the upper layer that develops mainly in the Southern California Bight in summer, and is connected to the CC allowing the recirculation of the cold water [*Lynn and Simpson*, 1987; *Di Lorenzo*, 2003]. The wind-driven upwelling caused by the equatorward alongshore wind, which is typically enhanced in summer, not only lifts the cold and saline water in lower layers but also generates a coastal jet and intensifies the equatorward flow of the CC [*Strub and James*, 2000]. Interannual variability of the current and water mass properties is also pronounced in the CCS, and this is caused by the changes in the source water, local winds, and/or ENSO events [*Bograd et al.*, 2015; *Zaba and Rudnick*, 2016; *Jacox et al.*, 2016].

The dynamics of the CCS have been studied over various spatial scales using both observations and numerical modeling. The mesoscale variability of the CCS was first recognized in shipboard observations such as the California Cooperative Oceanic Fisheries Investigations (CalCOFI) surveys [e.g., *Lynn and Simpson*, 1987]. *Kelly et al.* [1998] analyzed the data from surface drifters, satellite altimeters, and moored acoustic Doppler current profilers (ADCP) off northern California, and found that the seasonal enhancement and westward propagation of the eddy kinetic energy (EKE) reached a maximum from summer to fall, in accordance with the intensification of the equatorward flow. The EKE is concentrated in the wavelength range between approximately 240 and 370 km. The seasonal cycle of the altimeter-derived surface velocity field for the full CCS region was shown by *Strub and James* [2000], who found the spectral peak of the EKE around a wavelength of 300 km in an area 200–400 km from the coast. They explained this high EKE as a response to the meander of the equatorward jet and detached cyclonic and anticyclonic eddies detected around the jet

[*Strub and James*, 2000]. Based on velocity data from mooring arrays off Point Arena (38°54′N, 123°41′W), *Chereskin et al*. [2000] observed higher EKE near the continental slope (124°W) than in the offshore area (128°W).

This observed seasonal elevation and westward propagation of the mesoscale variances was reproduced by numerical models [*Haney et al*., 2001; *Di Lorenzo*, 2003] that used a finer resolution of O(10 km) than the first baroclinic Rossby radius of approximately 30 km in this region [*Chelton and Schlax*, 1996]. Although the generation of these mesoscale eddies was attributed to barotropic and baroclinic instabilities [*Di Lorenzo*, 2003], a finer-scale model with a resolution of O(1 km) indicated that there are vigorous interactions between the mesoscale and submesoscale motions [*Capet et al*., 2008]. However, observations with a resolution greater than that of the satellite altimetry are limited, especially in the interior below the surface. To validate the modeling results over mesoscale to submesoscale regions of the CCS, which is highly baroclinic, vertical profiles with a horizontal separation small enough to resolve mesoscale eddies and fronts are required.

Underwater glider observations differ from the conventional shipboard observations or Argo float arrays in that they can repeatedly acquire horizontally dense profiles from a targeted area [*Rudnick*, 2016b; *Rudnick et al*., 2016]. In the CCS, the California Underwater Glider Network (CUGN) has been operated using the Spray underwater glider along three CalCOFI lines (line 66.7 off Monterey Bay, line 80.0 off Point Conception, and line 90.0 off Dana Point) since 2006, with an approximate Nyquist wavelength of 5.6 km or less for 500 m-depth profiles [*Rudnick et al*., 2017]. In addition, Seaglider instruments recorded two sections off the Washington continental slope near the northern boundary of the CCS from 2003 to 2015, with an approximate Nyquist wavelength of 10 km or less for 1000 m-depth profiles [*Pelland et al*. 2013]. Because of their slow gliding speed, the spatial structure obtained from underwater glider data contains high-frequency signals such as internal waves; however, this is avoided if the measured properties are interpolated onto isopycnal surfaces [*Rudnick and Cole*, 2011].

Using data from the CUGN obtained between 2007 and 2011, *Todd et al*. [2012] investigated the thermohaline structure of the southern CCS and quantified annual variances of along-isopycnal salinity at mesoscale and submesoscale resolutions (30–200 and 6–30 km, respectively, by their definition) for the first time in this region. They found a distinct vertical structure in both the mesoscale and submesoscale variances, which were greatest within the remnant mixed layer, and showed a minimum near the 26.3 kg m^{-3} isopycnal and a local maximum around the 26.6–26.7 kg m^{-3} isopycnal. The spatial wavelet power spectra for the gradient of isopycnal salinity with respect to wavenumber k had a slope of k^0 (estimated by multiplying k^2 by the salinity spectra of k^{-2} originally presented in their paper) for all layers.

Pelland et al. [2013] analyzed the Seaglider data from off the Washington coast to examine subthermocline eddies that were generated from the CUC [*Garfield et al*., 1999; *Collins et al*., 2013]. Their observations, made between 2003 and 2009, detected 46 anticyclonic and 17 cyclonic eddies with average radii of 20.4 and 20.6 km, respectively. The water properties of the anticyclonic eddies at their core were warmer and saltier than the ambient water, which indicated that they were "Cuddies" [*Garfield et al*., 1999] originating from the CUC. Using a submesoscale-resolving numerical model for Monterey Bay, *Molemaker et al*. [2015] showed that subthermocline anticyclonic eddies similar to Cuddies develop from submesoscale elements that occur on the coastal side of the CUC and separate near areas of strong topographic curvature. These studies indicate that mesoscale features, such as cyclonic and anticyclonic eddies, are dynamically linked to smaller-scale variability in the CCS.

The distribution and mixing of tracers such as isopycnal salinity have also been studied in other regions. The slopes of the horizontal spectra of tracer gradients are often highlighted as they indicate the cascade of the variances across different scales. Observed spectral curves of the gradient of tracers over wavelength ranges from O(100 km) to O(1 km) were close to k^0 (k^{-2} for the tracer spectra), not only in the CCS [*Todd et al*., 2012], but also in many other areas such as the eastern subtropical North Pacific [*Ferrari and Rudnick*, 2000; *Cole et al*., 2010; *Callies and Ferrari*, 2013], central subtropical North Pacific [*Cole and Rudnick*, 2012], and the North Equatorial Current in the western North Pacific [*Schönau and Rudnick*, 2015] (except for the spectra of isopycnal salinity on the 25.5 kg m^{-3} isopycnal that was closer to k^1, where the variance reached a minimum). *Klymak et al*. [2015] analyzed O(1 km) data from Line P (the southern Gulf of Alaska), as well as an area north of the Hawaiian ridge, and obtained spice gradient spectra of $k^{0.6 \pm 0.2}$. The spice gradient spectra of Line P varied from around $k^{0.8}$ at depths of 40–60 m to around $k^{0.1}$ at 120–170 m [*Klymak et al*., 2015], which was assumed to be influenced by the CUC and its interaction with the topography that would generate Cuddies [*Pelland et al*., 2013].

Intensive surveys of lateral mixing processes were also conducted in the Sargasso Sea in the summer of 2011. The spectra of the isopycnal salinity gradient obtained from these surveys, which had a resolution of O(100 m), were again close to k^0 [*Kunze et al*., 2015]. As discussed in *Kunze et al*. [2015], the theoretical prediction of the tracer gradient spectra for the inertial range of quasi-geostrophic flows is $k^{1/3}$ at the surface and k^1 in the interior [*Scott*, 2006]; consequently, most of the spectra estimated in the above studies cannot be simply explained by the cascade in the quasi-geostrophic regime. On the other hand, *MacKinnon et al*. [2016] captured transitions of tracer spectra using high-resolution observations down to O(10 m) in the Bay of Bengal and the Arctic Ocean. The gradient spectra for the near-surface temperature (k^2 multiplied by the original temperature spectra) varied from k^0 (in the Bay of Bengal; k^{-1} in the Arctic Ocean) at scales of O(1–10 km) to k^1 at O(100 m), and further to $k^{1/3}$ at O(10 m).

Since *Todd et al*. [2012] presented the spatial structure of annual variances in isopycnal salinity for mesoscale and submesoscale regions of the CCS, the CUGN has accumulated a considerable amount of high-resolution (i.e., with a Nyquist wavelength of approximately 6 km) data that was recently compiled to obtain the climatology of the large-scale currents as well as the thermohaline structure [*Rudnick et al*., 2017]. In the present study, we aim to update the estimation of the fine-scale variances in the CCS by *Todd et al*. [2012] by analyzing the CUGN data, with an emphasis on the seasonal variability that was examined previously using satellite altimetry data [*Kelly et al*., 1998; *Strub and James*, 2000] at a resolution similar to, or greater than, the first baroclinic Rossby radius in this region. We also focus on the lateral structure of the fine-scale variances that are possibly related to fronts, currents, and detached eddies in the CCS [*Pelland et al*., 2013; *Klymak et al*., 2015; *Molemaker et al*., 2015].

We examine the variances over two main scale ranges: 30–60 km and 12–30 km. Although these are narrower than the 30–200 km and 6–30 km used by *Todd et al*. [2012], we also apply the terms mesoscale and submesoscale, respectively, to these ranges based on an assumed Rossby radius of approximately 30 km in the CCS [*Chelton et al*., 1996]. As explained in detail below, we restrict the upper bound of the mesoscale range to 60 km to allow us to estimate the variance near the lateral boundary without edge effects, and we set the lower bound of the submesoscale range to 12 km to avoid underestimation caused by the possible roll-off in the high wavenumber range. Using these variances without edge effects or roll-off, we are able to estimate the mean spectral slope over these scales together with their associated confidence intervals.

2. Data and Methods

2.1. Glider Data

The CUGN was launched in 2006 and has operated using Spray underwater gliders [*Sherman et al*., 2001] along three CalCOFI lines (line 66.7 off Monterey Bay, line 80.0 off Point Conception, and line 90.0 off Dana Point) for more than 10 years [*Rudnick et al*., 2017] (Figure 1). The gliders in the CUGN are equipped with conductivity-temperature-depth (CTD), chlorophyll *a* fluorescence, and acoustic Doppler sonar, and can dive from the surface down to 500 m or the seafloor (whichever is deeper) over a cycle of approximately 3 h that corresponds to horizontal intervals of 3 km or less. It usually takes 2–3 weeks for a glider to complete an out-and-back mission along the transects, which extend 350–500 km offshore. In 2016, the CUGN archived more than 400 transects and 95,000 profiles [*Rudnick et al*., 2017].

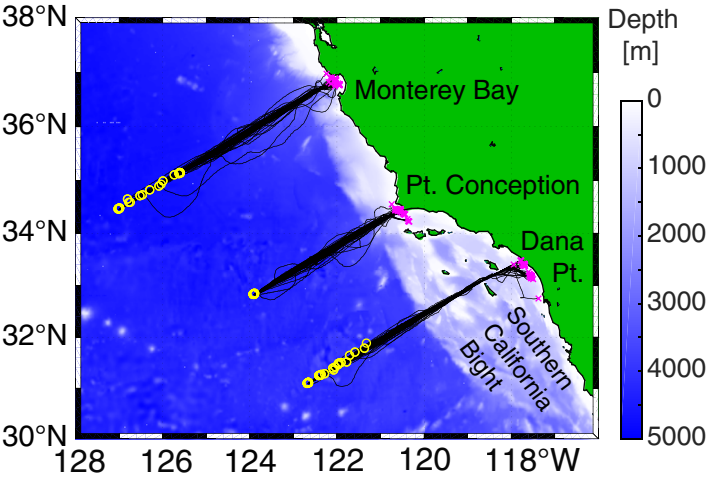

Figure 1. Tracks of CUGN underwater glider observations (black lines). Inshore and offshore ends shown with magenta crosses and yellow circles, respectively.

We analyzed isopycnal salinity along the 25.0–26.9 kg m^{-3} isopycnals as in previous studies [e.g., *Rudnick et al*., 2011], which excluded signals of internal

wave heaving. The 25.0 kg m^{-3} isopycnal surface is usually observed above a depth of 100 m, and partly outcrops in winter and spring on the coastal side. The 26.9 kg m^{-3} isopycnal is almost the deepest isopycnal surface constantly available for 500 m profiles [*Rudnick et al*., 2017]. The raw data were manually quality controlled to eliminate bad values and then binned at intervals of 10 m for depths of 10–500 m [*Rudnick*, 2016a]. These isobaric data then interpolated onto the isopycnal surfaces at an interval of 0.05 kg m^{-3}. Then, following *Todd et al*. [2012], the isopycnal data from the dive points were projected onto the CalCOFI lines and interpolated along the line at an interval of 0.5 km. Data with an offset from the CalCOFI lines greater than 30 km were not used. Also, unlike *Todd et al*. [2012], we did not use objective mapping to fill missing data, but instead used a simple linear interpolation along the lines between only two data points. Because of the interpolation, the effective horizontal resolution could be reduced from 3 to 6 km at most (Nyquist wavelength of 6–12 km). After smoothing any discontinuities, possibly caused by the projection, using a fifth-order Butterworth low-pass filter with a half power of 3 km, we calculated the along-track isopycnal salinity gradient data that were used for the wavelet analysis.

To obtain the seasonal fine-scale variances in their mean state, we used the data for the periods 2007–2013 for lines 80.0 and 90.0 (operation started in October 2006), and 2008–2013 for line 66.7 (operation started in April 2007), as did *Rudnick et al*. [2017]; data from 2014–2016 were not used because extreme warming occurred during this period [*Zaba and Rudnick*, 2016]. These transects were compiled by season; i.e., winter (December, January, and February), spring (March, April, and May), summer (June, July, and August), and fall (September, October, and November). The "date" of each transect, which take 1–1.5 weeks, was determined from the midtime of the transect. The number of available transects for each season along each line was between 17 and 30, with the greatest (smallest) number being along line 80.0 (66.7), and seasonal differences were relatively small (Figure 2).

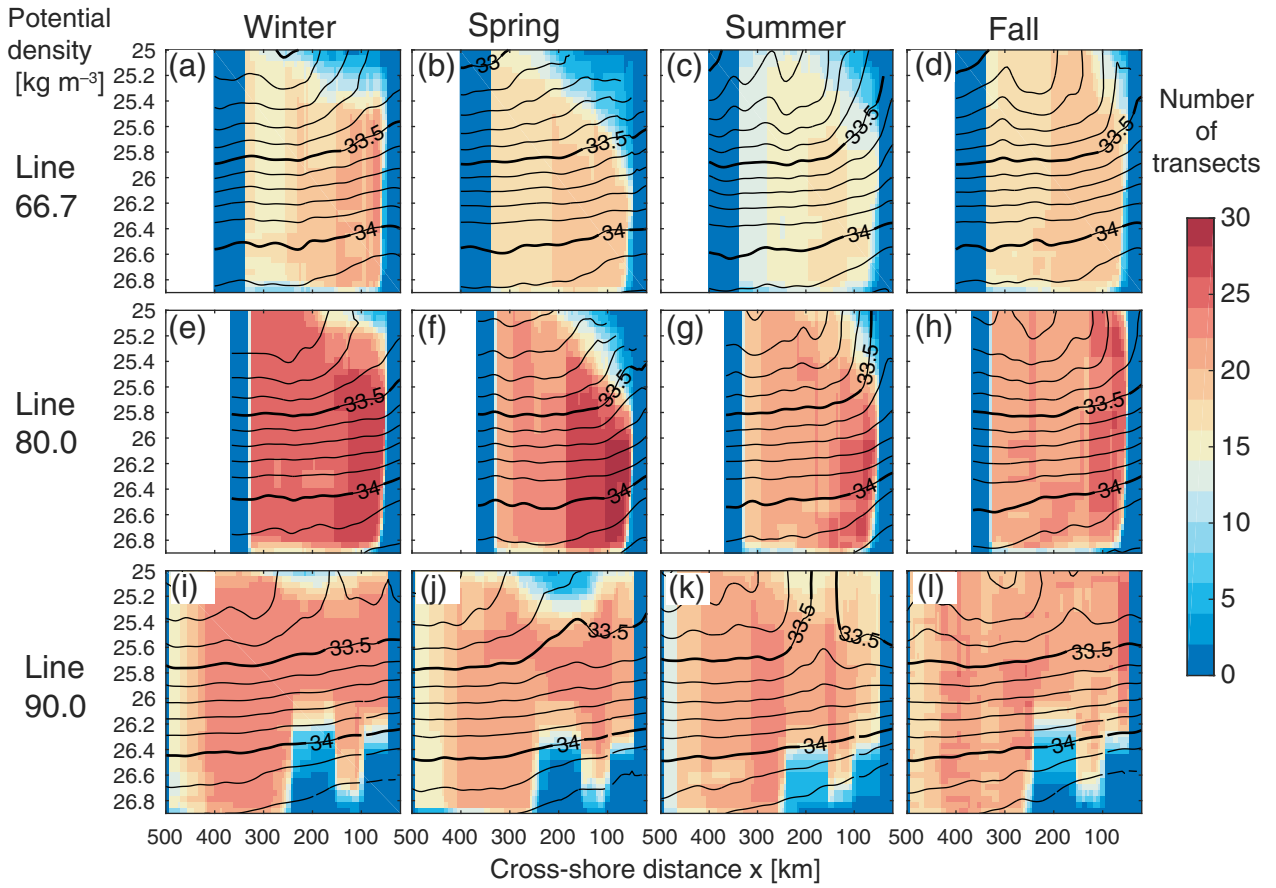

Figure 2. Number of available glider transects in each season along each line (color). Horizontal and vertical axes denote cross-shore distance and potential density, respectively. Contour lines indicate the climatological salinity and are based on data presented in *Rudnick et al*. [2017] and averaged over each season.

2.2. Wavelet Analysis

The spatial structure of the fine-scale variances was estimated using wavelet analysis [*Torrence and Compo*, 1998] as in previous studies [*Ferrari and Rudnick*, 2000; *Todd et al*., 2011; *Schönau and Rudnick*, 2015]. We used the isopycnal salinity gradient along the transect, instead of the isopycnal salinity, as the spectra are equivalent to those of salinity if multiplied by the square of the wavenumber k^2. We took this approach mainly because of the expectation of an approximately k^0 slope for the gradient spectra, from which it is easier to discuss deviations. The continuous wavelet transform is defined as the convolution of the data (in this case the isopycnal salinity gradient with respect to the offshore distance) with a scaled mother wavelet, which in practice is calculated using the inverse Fourier transform of the products of the Fourier-transformed data and the mother wavelet [*Torrence and Compo*, 1998]. By selecting the Morlet wavelet $\psi(x) = \pi^{-1/4}\exp(ik_0x)\exp(-x^2/2)$ for the mother wavelet, where the nondimensional wavenumber k_0 was set to six [*Torrence and Compo*, 1998], we obtained the wavelet transform $W_t(s,x,d)$ of the horizontal gradient of isopycnal salinity, where s, x, and d are the cross-shore scale, the distance from the shore, and the potential density (vertical coordinate), respectively. Subscript t indicates the midtime of the observation for continuous segments. The spatial distribution of wavelet power spectra for a single transect was then obtained as $|W_t(s,x,d)|^2$.

Because of the nature of the convolution, the estimated wavelet power spectra near the end points within the Gaussian decay scale of the scaled Morlet wavelet $\psi(x/s) = \pi^{-1/4}\exp(ik_0x/s)\exp\{-(x/s)^2/2\}$ are not valid (due to edge effects). Following *Torrence and Compo* [1998], we defined valid and invalid regions of the wavelet power spectra using the distance $2^{1/2}s$ from the end points, where wavelet power decays down to e^{-2}. For example, variance with a scale of 100 km is available for a region 141 km from the end points. To capture the variability near the continental shelf, where the poleward CUC and the equatorward CC were observed [*Rudnick et al*., 2017], we focused mainly on the variance at scales below 60 km. Considering also the lower bound of 12 km mentioned above, we calculated variances for 30–60 and 12–30 km using the following method, and which we termed mesoscale and submesoscale, respectively.

The scale-averaged wavelet power $P_{i,t}(x,d)$ was calculated from the wavelet power spectra $|W_t(s,x,d)|^2$ at four scale ranges, namely, mesoscale (ms: 30–60 km), submesoscale (sm: 12–30 km), upper submesoscale (usm: 12–20 km), and lower submesoscale (lsm: 20–30 km), and is denoted by the subscript i. We note that these scale-averaged wavelet powers are equivalent to the distribution of the variance for a unit wavelength range. Seasonal mean power $\overline{P_{i,j}}(x,d)$ at each scale range i for season j was then obtained from the ensemble mean. To examine the lateral structure of the fine-scale power, we further divided $\overline{P_{i,j}}(x,d)$ by the total variance ${\sigma_d}^2$ of the isopycnal salinity gradient to obtain the variance-normalized scale-averaged wavelet power $\overline{\Phi_{i,j}}(x,d)$, where σ_d was calculated by averaging the variances directly calculated from the transect data.

The ratio of the two scale-averaged powers is related to the spectral slope. Given that the spectrum is $P \sim k^b$ over a wavenumber range $[k_1, k_2]$, then the spectral slope b can be obtained from:

$$b = \frac{\log(P_2/P_1)}{\log(k_2/k_1)}, \tag{1}$$

using the mean powers P_1 and P_2 at k_1 and k_2, respectively. We estimated the mean spectral slope b over the combined mesoscale to submesoscale (12–60 km) range as well as the submesoscale (12–30 km) range, using pairs of seasonal-mean scale-averaged powers $\overline{P_{i,j}}(x,d)$. As we sampled the wavelet scales s on a logarithmic scale, as in *Torrence and Compo* [1998], the mean logarithmic wavelet scale $\log s_i$ within a scale bin i was obtained from the log-means of the scales within the bin. The mean wavelet wavelength k_i was then calculated as $k_i = 1/s_i$, which is 1.03 times the Fourier wavelength in our case using the Morlet wavelet with the nondimensional wavenumber $k_0 = 6$ [*Torrence and Compo*, 1998]. The mean wavenumbers expressed in cycles per kilometer (cpkm) at the mesoscale, submesoscale, upper submesoscale, and lower submesoscale were 1/43, 1/19, 1/25, and 1/15 cpkm, respectively.

The confidence intervals of the power spectrum were estimated by assuming the χ^2 distribution. The degrees of freedom for the mean powers $\overline{P_{i,j}}$ and $\overline{\Phi_{i,j}}$ were calculated by multiplying N (the number of available segments) by a factor determined from the mother wavelet and the integration over the scales

[*Torrence and Compo*, 1998], which, in the present study, was 1.90, 2.41, 1.43, and 1.58 for the mesoscale, submesoscale, upper submesoscale, and lower submesoscale power, respectively. If, for example, $N = 25$ (see Figure 2 for the number of transects), the 95% confidence interval (2.5%–97.5%) of the power spectrum is 69%–156% and 72%–148% for the mesoscale and submesoscale, respectively. For the ratio of the two scale-averaged powers, the confidence interval is given by the F distribution. The confidence interval of the exponent b over a scale range $[k_1, k_2]$ is thus defined as $\log(F)/\log(k_2/k_1)$. Although the spatial distribution of the exponent b could be estimated, we further averaged $\overline{P_{i,j}}(x, d)$ over cross-shore regions to obtain the vertical profiles of the mean powers $\overline{P_{i,j,X}}(d)$ for inshore ($x < 150$ km for lines 66.7 and 80.0, but $x < 200$ km for line 90.0) [*Rudnick et al*., 2017] and offshore ($x \geq 150$ km for lines 66.7 and 80.0, but $x \geq 200$ km for line 90.0) [*Rudnick et al*. 2017) areas with greater accuracy, where the subscript X denotes either inshore or offshore areas. The increase in the effective degrees of freedom generated by using this spatial averaging was estimated by dividing the ranges by 30 km, which is slightly greater than the decorrelation scale of this region calculated by *Klymak et al*. [2015].

3. Results

Both the mesoscale (30–60 km) and submesoscale (12–30 km) power show marked three-dimensional variability with respect to potential density and along and cross-shore distance, which also fluctuate seasonally. We consider the spatiotemporal variability of the submesoscale and mesoscale power in section 3.1, and then present spectral curves and slopes over these ranges in section 3.2.

Cross sections of the fine-scale variances with respect to cross-shore distance and potential density were overlaid with the salinity or geostrophic velocity climatology by *Rudnick et al*. [2017]. As presented in *Rudnick et al*. [2017], the subsurface isopycnals are lifted close to the surface by the wind-driven upwelling that typically occurs in spring and summer and become warmer, resulting in an increase in the isopycnal salinity.

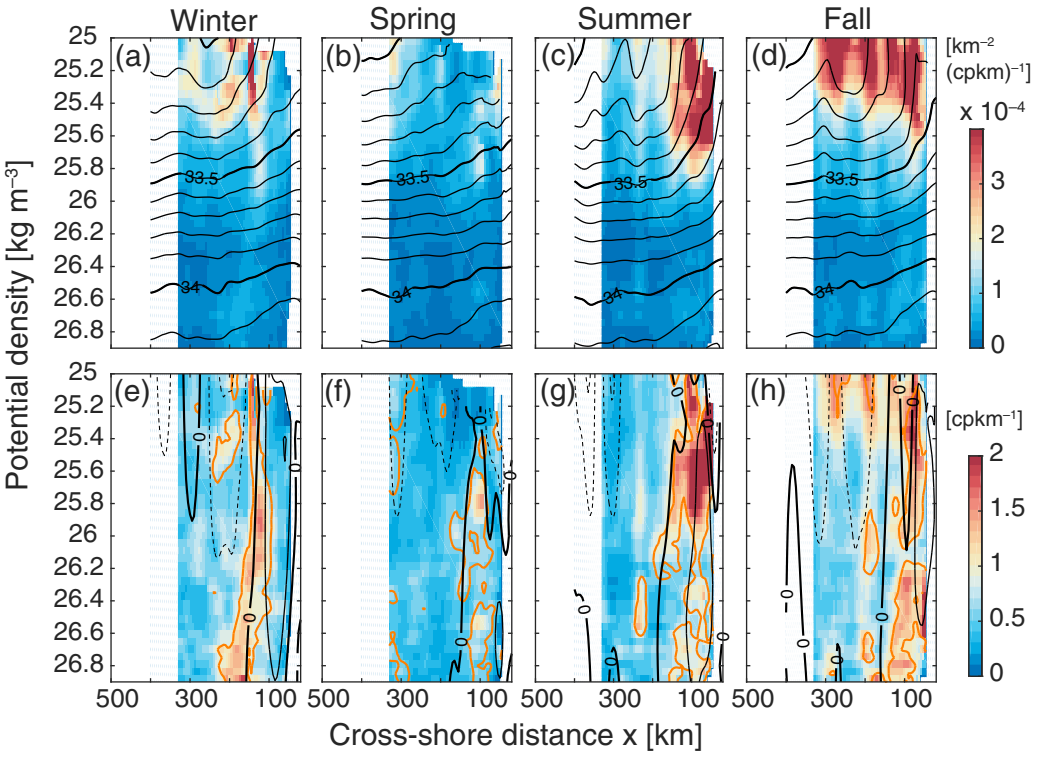

Figure 3. Submesoscale power of isopycnal salinity gradient along line 66.7. Raw values and those normalized by the isopycnal variance are shown in the top and bottom plots, respectively, and the powers averaged over winter, spring, summer, and fall are shown in the four columns. Black contours in the top and bottom plots are the climatological salinity and geostrophic velocity from *Rudnick et al*. [2017], and orange lines in the bottom plot denote the lower 5% bound of the confidence interval. For the geostrophic velocity, poleward (equatorward) components are shown with solid (dashed) lines with a contour interval of 5 cm s^{-1}.

Although this salinification is obviously not caused by isopycnal processes, we use this signal in the isopycnal coordinate to detect the upwelling of isopycnals toward the surface, and we use the term "upwelling cell" for this signal.

3.1. Submesoscale and Mesoscale Power

The submesoscale power at 12–30 km was strong in the upper layer, along line 66.7 off Monterey Bay, on the inshore side of the transect, and from summer to fall (Figure 3, top row). The elevated power in the upper layer was observed typically above the 25.8 kg m^{-3} isopycnal, became a minimum around the 26.3 kg m^{-3} isopycnal, and then increased again with increasing depth, which is consistent with *Todd et al.* [2012]. The level of variance in the upper layer was relatively high along line 66.7 (Figure 3) but low along line 90.0 (Figure 5). The total (areal, vertical, and seasonal) mean power along line 66.7 was 1.4 times that along line 80.0 (Figure 4) and 2.3 times that along line 90.0.

Summer and fall were the seasons of the strongest submesoscale power. The poleward CUC transport of warm and saline water strengthens during these seasons and elevates isopycnal salinity on the inshore side, which leads to the formation of salinity fronts on the isopycnals, while it is likely that the extremely strong gradient in the upper layers is also caused by the atmospheric near-surface heating/mixing (Figures 3c, 3d, 3g, 3h, 4c, 4d, 4g, 4h, and 5c, 5d, 5g, 5h). In summer, elevated power that was significantly stronger than the isopycnal means was observed around the isopycnal salinity front that corresponds to the core of the poleward flow of the CUC along line 66.7 (Figure 3g), and around the front and its offshore side along lines 80.0 and 90.0 (Figures 4g and 5g). The elevated variances in the upper layer, typically above the 25.5 kg m^{-3} isopycnal, spread seaward in fall (Figures 3h, 4h, and 5h).

In winter, when the large-scale cross-shore salinity gradient is moderate, the power was also moderate (Figures 3a, 4a, and 5a). Elevated power was not necessarily concentrated around the front, but some was

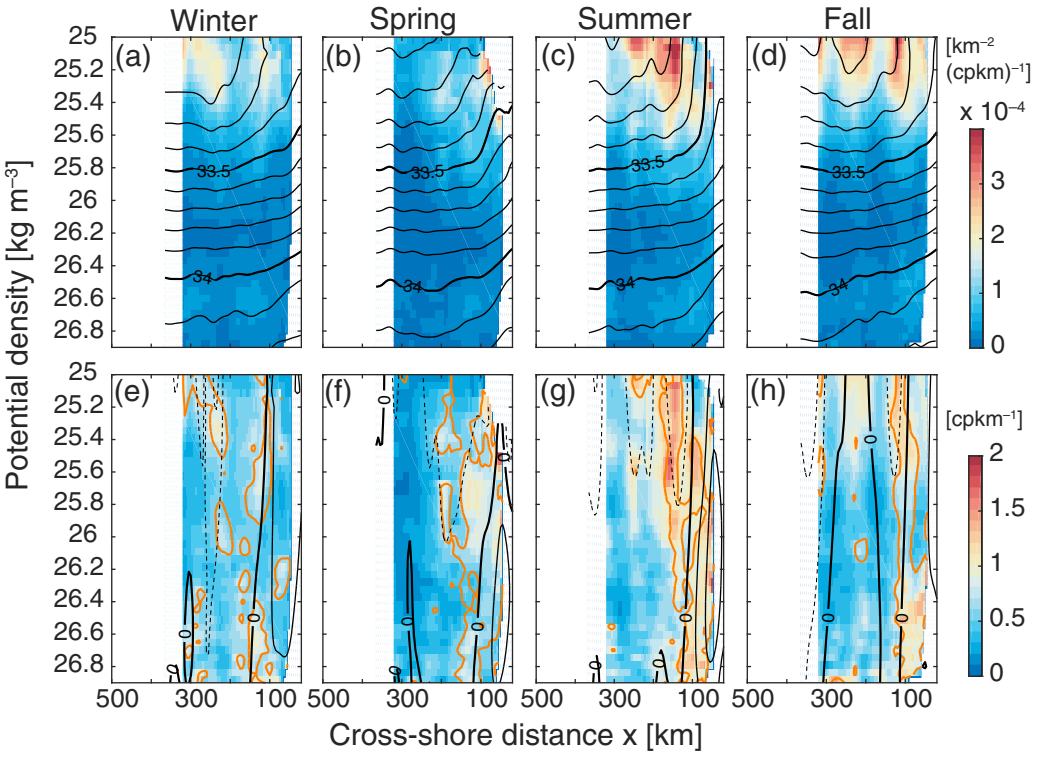

Figure 4. Submesoscale power of isopycnal salinity gradient along line 80.0. Raw values and those normalized by the isopycnal variance are shown in the top and bottom columns, respectively, and the powers averaged over winter, spring, summer, and fall are shown in the four columns. Black contours in the top and bottom plots are the climatological salinity and geostrophic velocity from *Rudnick et al.* [2017], and orange lines in the bottom plot denote the lower 5% bound of the confidence interval. For the geostrophic velocity, poleward (equatorward) components are shown with solid (dashed) lines with a contour interval of 5 cm s^{-1}.

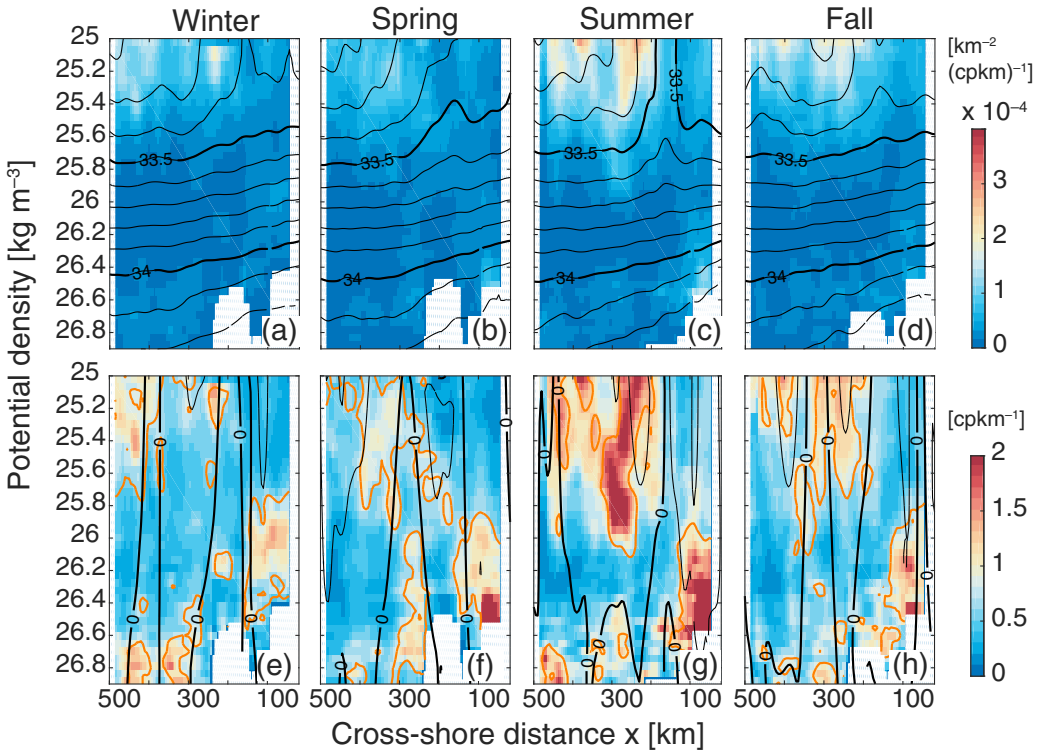

Figure 5. Submesoscale power of isopycnal salinity gradient along line 90.0. Raw values and those normalized by the isopycnal variance are shown in the top and bottom columns, respectively, and the powers averaged over winter, spring, summer, and fall are shown in the four columns. Black contours in the top and bottom plots are the climatological salinity and geostrophic velocity from *Rudnick et al*. [2017], and orange lines in the bottom plot denote the lower 5% bound of the confidence interval. For the geostrophic velocity, poleward (equatorward) components are shown with solid (dashed) lines with a contour interval of 5 cm s^{-1}.

distributed far offshore from the front, such as along lines 80.0 (Figure 4e) and 90.0 (Figure 5e), which had possibly propagated from areas around the front. Although the submesoscale power was weakest in spring, slight elevations in areas similar to the summer enhancements are evident in Figures 3b, 4b, and 5b.

Along line 66.7 in winter, a prominent vertical band of normalized power penetrating down to the 26.9 kg m^{-3} isopycnal was detected on the offshore side of the salinity front, which corresponds to the boundary between the equatorward and poleward flows (Figure 3d). We suggest that this structure is related to interaction between the equatorward CC and the poleward CUC that has a semiannual cycle with a weak peak in winter [*Rudnick et al*., 2017], and we will discuss this further in section 4.

In the lower layer of line 90.0, the normalized power was almost always elevated in the Southern California Bight (inshore 200 km of line 90.0). This was especially enhanced in summer (Figure 5g). The lower-layer peak in summer along line 90.0 was clearly separated from the upper-layer peak on the onshore side of the front. The lower-layer peaks in lines 66.7 and 80.0 also developed near the coast (Figures 3g and 4g), but differed from line 90 in that they were connected to the upper-layer peaks.

The overall pattern of the mesoscale power (Figure 6) at 30–60 km was similar to that of the submesoscale power (12–30 km; Figures 3–5), although there was less data available near the inshore and offshore ends because of the edge effect. Nevertheless, the detailed structure at the two scales differed. For example, for line 66.7 in winter (Figure 6a), the strong vertical band offshore of the front (100–200 km) observed for the submesoscale power (Figure 3a, d) did not appear at the mesoscale; and the elevated power was observed in the upper layer in an area farther offshore (200–300 km) and did not penetrate the lower layer. For line 90.0 in summer (Figure 6k), the elevated power offshore of the upwelling cell spread widely, and the extent of the lower-layer peak on the inshore side was narrower than that of the mesoscale power (Figure 5g).

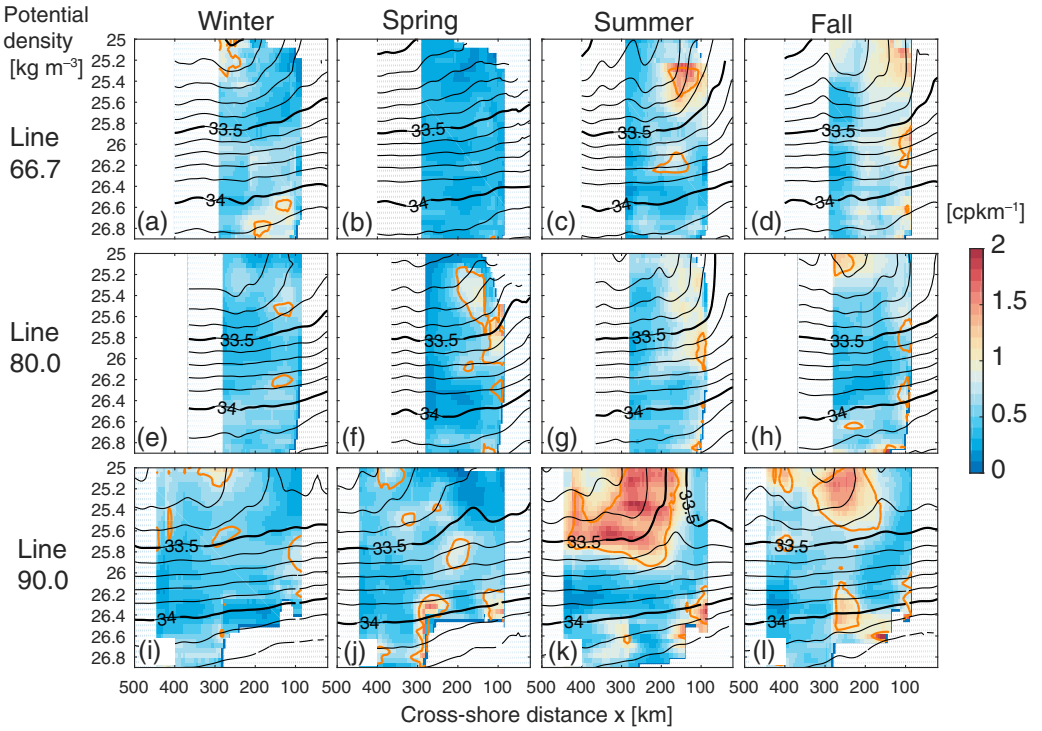

Figure 6. Mesoscale power of the isopycnal salinity gradient normalized by the isopycnal variance in the four seasons along the three lines. Black contours are the climatological salinity from *Rudnick et al*. [2017], and orange lines in the bottom plot denote the lower 5% bound of the confidence interval.

3.2. Spectral Slopes

We calculated the mean power spectra of the isopycnal salinity gradient for the inshore ($x < 150$ km for lines 66.7 and 80.0, but $x < 200$ km for line 90.0) and offshore ($x \geq 150$ km for lines 66.7 and 80.0, but $x \geq 200$ km for line 90.0) areas over the scale range of 12–60 km (Figures 7 and 8). Although the level of the power is high in the upper layer and a minimum around 26.3 kg m^{-3}, which is consistent with Figures 3–6, the slopes and curvature of the spectra cannot be simply categorized using isopycnals, seasons, lines, or areas (inshore or offshore). Some spectral curves, such as those of the inshore winter upper layer along line 66.7 (Figure 7a), inshore summer lower layer along line 80.0 (Figure 7g), and offshore summer upper layer along line 80.0 (Figure 8g) show a slight positive trend (positive slope); however, a negative trend is also observed, such as for the inshore summer upper layer along line 90.0 (Figure 7k). Except for some narrow portions, the spectral curves are not parallel to the k^{+1} curve.

The mean slopes over the submesoscale and mesoscale ranges (12–60 km) were obtained from the ratio of the mean spectra, separately averaged over submesoscale (12–30 km, centered at 19 km) and mesoscale (30–60 km, 43 km) and also over lateral extent (Figure 9). The mean $\pm$ standard deviation of the mean slope of all data was 0.19 ± 0.27 (the range of ± 1 sigma corresponds to the 14th–86th percentiles), and those for the inshore and offshore areas were 0.25 ± 0.32 (14%–86%) and 0.14 ± 0.19 (16%–84%), respectively. Significantly positive values (those where the lower bound of the confidence interval exceeded zero) occurred for the inshore winter-fall along line 66.7 (Figure 9a), inshore winter lower layer along line 90.0 (Figure 9c), offshore spring intermediate layer along line 66.7 (Figure 9d), offshore summer upper layer along line 80.0 (Figure 9e), and offshore winter lower layer along line 90.0 (Figure 9f). The proportions of the significantly positive values were 35% for the inshore area and 31% for the offshore area, whereas those exceeding 1/3 occurred only in the inshore area with a proportion of 8.8%, mostly in winter along line 66.7. Significantly negative values occurred less frequently than the significantly positive values: 4.0% for the inshore area and 2.4% for the offshore area.

As outlined in section 1, dimensional arguments predict that the slope of the tracer gradient spectra is scaled by k^{+1} in the inertial range of quasi-geostrophic flows, whereas most of previous observations found

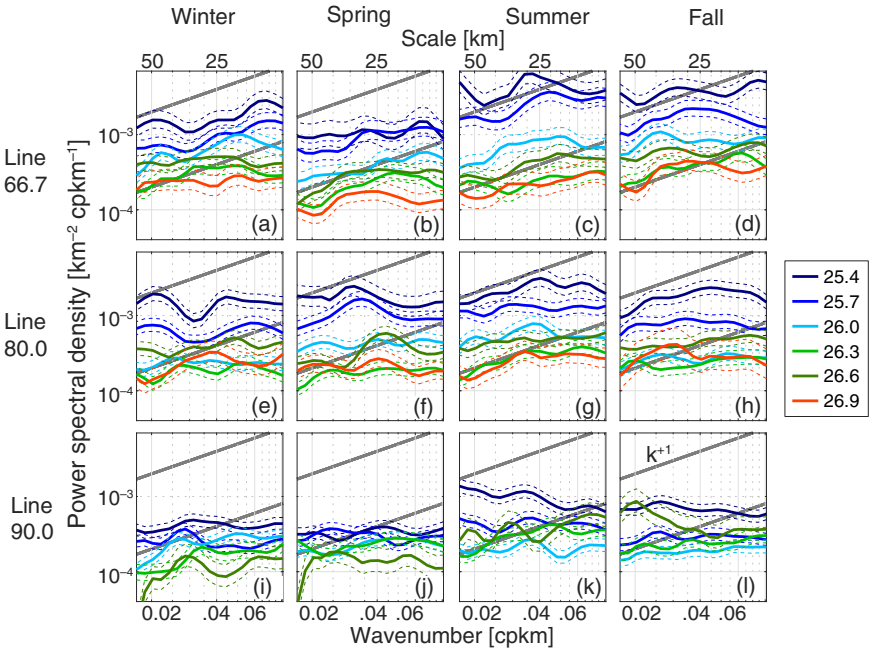

Figure 7. Power spectral density of isopycnal salinity gradient over the 1/60–1/12 cpkm range on the inshore side ($x < 150$ km for lines 66.7 and 80.0, but $x < 200$ km for line 90.0) in the four seasons along the three lines. Thick gray lines are parallel to k^{+1}.

k^0 slope over the scales of O(100 km) to O(1 km). However, given that energy input occurs around the baroclinic Rossby radius, which we assumed to be 30 km according to *Chelton et al.* [1996], the inertial range should be below this energy injection scale. Therefore, we calculated spectra at the submesoscale range, using the mean powers over the lower submesoscale (12–20 km, centered at 15 km) and upper submesoscale (20–30 km, centered at 25 km; Figure 10).

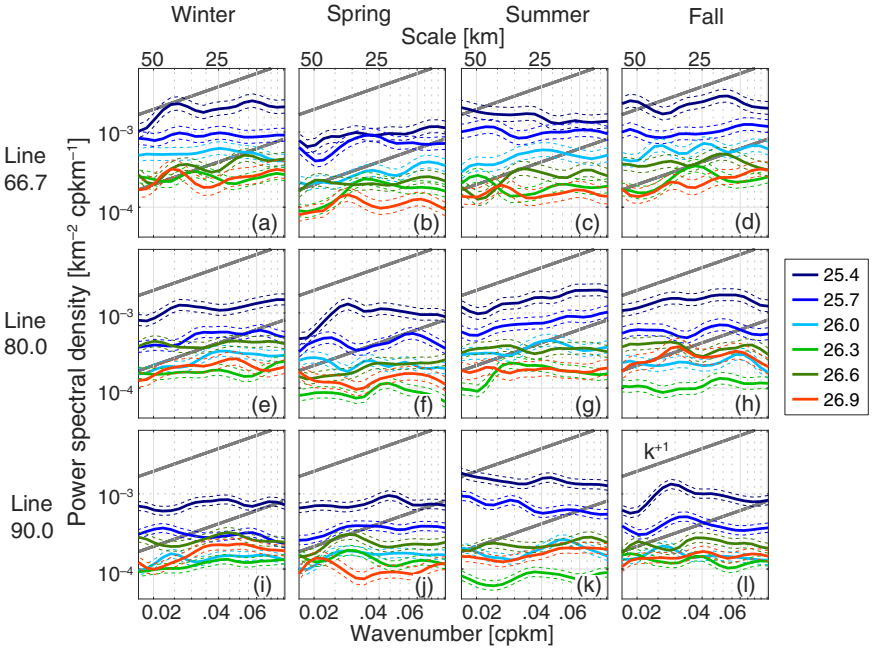

Figure 8. Power spectral density of isopycnal salinity gradient over the 1/60–1/12 cpkm range on the offshore side ($x \geq 150$ km for lines 66.7 and 80.0, but $x \geq 200$ km for line 90.0) in the four seasons along the three lines. Thick gray lines are parallel to k^{+1}.

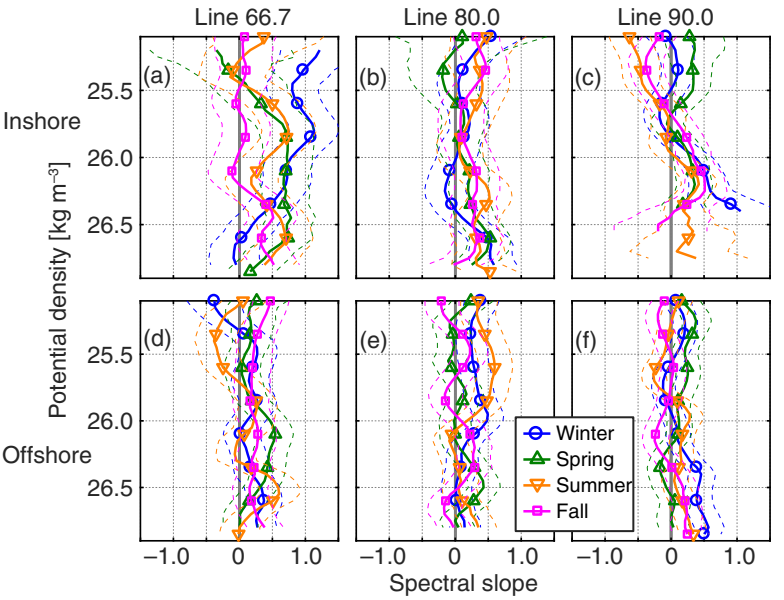

Figure 9. Mean vertical profiles of the spectral slope calculated from the ratio of the submesoscale (12–30 km, mean scale of 19 km) and mesoscale (30–60 km, mean scale of 43 km) power. Those for the inshore (offshore) areas are shown in the top (bottom) rows, and those for lines 66.7, 80.0, and 90.0 are shown in the left, center, and right columns, respectively. Thick lines with symbols indicate mean estimates based on 5 point vertically smoothed ($\pm$ 0.1 kg m^{-3}) moving average, and thin lines are the corresponding 95% confidence intervals.

Compared with the spectra over mesoscale and submesoscale (12–60 km, Figure 9), the estimated spectral slope was distributed closer to zero (Figure 10). The mean $\pm$ standard deviation of the mean slope of all data was -0.025 ± 0.32 (the range of $\pm$ 1 sigma corresponds to the 15th–87th percentiles), and those for the inshore and offshore areas were 0.015 ± 0.37 (15%–89%) and -0.065 ± 0.26 (14%–82%), respectively. Significantly positive values were observed almost exclusively in the inshore winter upper layer along line 66.7 (Figure 10a), inshore winter lower layer along line 90.0 (Figure 10c), and offshore upper layer along line

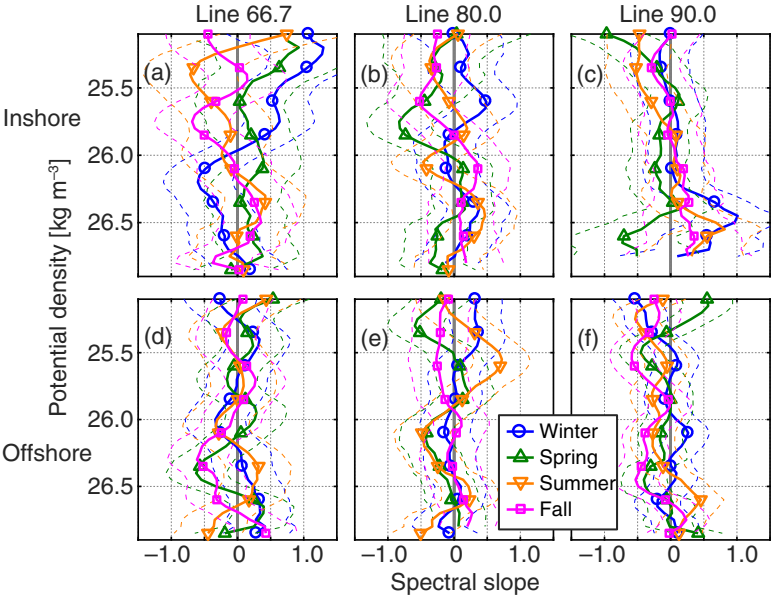

Figure 10. Mean vertical profiles of the spectral slope calculated from the ratio of the lower submesoscale (12–20 km, mean scale of 15 km) and upper submesoscale (20–30 km, mean scale of 25 km) power. Those for the inshore (offshore) areas are shown in the top (bottom) rows, and those for lines 66.7, 80.0, and 90.0 are shown in the left, center, and right columns, respectively. Thick lines with symbols indicate mean estimates based on 5 point vertically smoothed ($\pm$ 0.1 kg m^{-3}) moving average, and thin lines are the corresponding 95% confidence intervals.

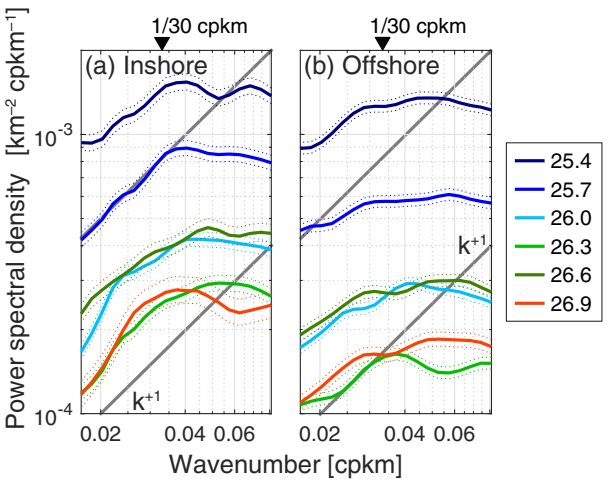

Figure 11. Mean power spectral density of isopycnal salinity gradient averaged over the three lines and the four seasons: (a) inshore side ($x < 150$ km for lines 66.7 and 80.0, but $x < 200$ km for line 90.0) and (b) offshore side ($x \geq 150$ km for lines 66.7 and 80.0, but $x \geq 200$ km for line 90.0). Thick gray lines are parallel to k^{+1}.

80.0 (Figure 10e). In the inshore and offshore areas, 8.6% and 7.2%, respectively, of the data were significantly greater than zero, which are slightly greater proportions than the upper percentile of the confidence interval (2.5%). Spectral slopes that were significantly greater than 1/3 accounted for 2.1% (0.70%) of the available data in the inshore (offshore) area. Significantly negative values accounted for 9.7% (16%) of the available data in the inshore (offshore) area, but those significantly smaller than 1/3 were less than 1.0% for both areas.

When averaged over the three lines and four seasons, the mean spectral curves show the transition of the slope between mesoscale and submesoscale wavenumber ranges (Figure 11). This feature is clearer in the inshore area, where positive slopes rapidly turn to flat in a wavenumber range from 0.025 (1/40) to 0.05 (1/20) cpkm (Figure 11a). The transition is gradual in the offshore area, especially in the upper layer (Figure 11b). Some of the positive slopes in a low wavenumber side are somehow close to k^{+1}, such as the spectrum at 25.7 kg m^{-3} isopycnal in the inshore area, we cannot conclude that this is consistent with the theoretical prediction, as the energy input might occur around the baroclinic Rossby radius, generally above the range of the positive slopes.

4. Discussion and Conclusions

The high-horizontal-resolution underwater glider data from 2007 to 2013 revealed the large spatial and seasonal variability at the submesoscale (12–30 km) and mesoscale (30–60 km) in the CCS (Figures 3–6). Our results are consistent with those of *Todd et al*. [2012], who presented the mean structure of the fine-scale variances in the CCS, but the accumulation of data enabled us to obtain the seasonal means for the first time. The fine-scale power was elevated mainly around the salinity front and its offshore side in summer, and spread over the offshore areas through fall and winter. The average level of the variances was highest (lowest) along line 66.7 (90.0). The vertical structure was consistent with *Todd et al*. [2012] in that the minimum was observed around the 26.3 kg m^{-3} isopycnal.

The vertical profiles of the submesoscale and mesoscale power can be explained by the large-scale horizontal gradient of the isopycnal salinity compiled by *Rudnick et al*. [2017]. As seen in the climatological salinity distributions of the isopycnal surfaces (Figures 3–5, contours in top rows), contours of isopycnal salinity are strongly slanting in the upper layer, which indicates the large horizontal gradient. The slope of the contours becomes flatter until around the 26.3 kg m^{-3} isopycnal, and then begins to slant again on the inshore side. The horizontal gradients observed in the climatology [*Rudnick et al*., 2017] are most probably caused by the front that divides the different water masses. The upper gradient, above the 26.3 kg m^{-3} isopycnal, forms between the subarctic water transported by the CC and the equatorial water transported by the CUC, which is also locally modified by atmospheric forcing through the development of upwelling cells. The lower gradient, below the 26.3 kg m^{-3} isopycnal, most probably forms between the CUC and the North Pacific Intermediate Water (NPIW) [*Talley*, 1993; *Yasuda*, 1997], which is characterized by a salinity minimum around the 26.8 kg m^{-3} isopycnal, spreading from the central subtropical North Pacific [*Cole and Rudnick*, 2012] to the CCS. The fine-scale fluctuations that first developed at these fronts are intensified mainly in summer through instabilities, although they could be redistributed along isopycnal surfaces by the westward propagation of mesoscale eddies with core waters and smaller-scale variability around the eddies. We note that the propagation of tracer variability does not occur in the linear regime, which contrasts with the kinetic energy observed by *Kelly et al*. [1998].

The 26.3 kg m^{-3} isopycnal figures prominently in our results as a minimum of mesoscale and submesoscale variance. This isopycnal is also the one that shoals the most during upwelling in spring [*Rudnick et al*., 2017]. As such, this surface acts as a partition between an upper level that is directly affected by wind-driven upwelling and a lower level that is part of the upwelling cell but is less driven by the frictional effects of wind. The 26.3 kg m^{-3} isopycnal is located between 150 and 200 m on average. In comparison, the pycnocline tends to be in the upper 50 m nearshore, and even outcrops during upwelling season. So wind-driven upwelling penetrates beneath the pycnocline, and the largest upwelling displacements are deeper. The different regimes on either side of the 26.3 kg m^{-3} isopycnal may influence the distribution of thermohaline tracers, as reflected in the salinity variance presented here.

The mean spectral slope over the 12–60 km range, calculated from the ratio of the mean powers at 19 and 43 km, showed large spatial and seasonal variability with a mean and standard deviation of -0.19 ± 0.27 (Figure 9). Approximately 30% to 35% of the slope values were significantly greater than zero, which differs from the results of *Todd et al*. [2012] who reported a gradient spectral slope of k^0 (k^{-2} for the salinity spectra) in the CCS. However, taking the ratio of the powers at 15 and 25 km, we obtained spectral slopes that were mostly not significantly different from zero. We thus confirm that the spectral power of the salinity gradient increases with increasing wavenumber (positive exponent) at the mesoscale (30–60 km), and then becomes almost constant ($\sim k^0$) at the submesoscale (12–30 km), as was also suggested in the spectral curves (Figures 7, 8 and 11). Although the ranges used to calculate the spectra were different, this k^0 slope has also been obtained in other areas [e.g., *Ferrari and Rudnick*, 2000*; Cole et al*., 2010*; Cole and Rudnick*, 2012*; Callies et al*., 2013*; Schönau and Rudnick*, 2015].

The mean spectral slope that is close to the k^0 slope estimated for the submesoscale differs from the dimensional argument that predicts a k^{+1} slope. As discussed in *Callies et al*. [2013], the k^0 slope for tracer gradient spectra (k^{-2} for tracer spectra) is expected for discontinuities. If two different water masses are transported by currents to form a sharp front then the tracer spectra would reflect this frontal structure, which means that a tracer is injected at this scale. This differs from the assumption of deriving a k^{+1} slope that considers a smaller scale than the tracer injection [e.g., *Vallis*, 2006]. Given that the gradient of the salinity at the front is approximated by a Gaussian function $S_x(x) \sim \exp(-x^2/L^2)$, then the salinity gradient spectrum becomes $\hat{S}_x(k) \sim \exp(-\pi^2 L^2 k^2)$. If the front is sharp enough that πL is smaller than the target spatial scale of $1/k_1$, the spectrum around k_1 can be approximated as $\hat{S}_x(k) \sim 1-\pi^2 L^2 k^2$. The spectrum would become close to flat if $\pi L \ll 1/k_1$, or become negative for a moderately small L that might be compensated for by the k^{+1} slope caused by the stirring without the external tracer injection. Therefore, it is possible that sharp fronts substantially narrower than 30 km/π ($\sim$ 10 km) cause the flat spectrum.

A single sharp front can result in a nearly flat spectrum, but a flat spectrum itself is not necessarily caused by a single sharp front, but can also be generated by white noise. To examine whether or not the flat spectra at the submesoscale were caused by white noise, we examined the phase difference between the scale-averaged wavelet transforms at the upper (25 km) and lower (15 km) submesoscale. If the salinity gradient was caused by white noise, then the phase difference would be random. On the other hand, if the salinity gradient is represented by a sharp single peak, then the phase difference would be close to zero. We tested this anisotropy using the Rayleigh test [*Fischer*, 1995]. Unit vectors constructed from the angle of the two wavelet transform obtained from single transects were averaged and then compared with the 95% confidence limit (Figure 12): if the mean of the unit vectors is greater than the 95% limit, then phases of the two wavelet transforms are not random. Our results showed that the values were generally around the 95% limit (Figure 12), which indicates that not all salinity gradient records were random. In contrast, the mean of the unit vectors calculated from the phase difference between the mesoscale and submesoscale wavelet transforms were mostly smaller than the 95% limit (not shown). We suggest that the submesoscale salinity variability is generally caused by a small number of sharp fronts that are less than 10 km wide, whereas the mesoscale salinity variability includes more random fluctuations that result in the bluer spectra.

As mentioned in section 3, the fine-scale powers and their associated ratios shown in Figures 3–11 exhibit some spatiotemporal variability. One notable structure of the submesoscale power and the spectral slope was found along line 66.7 in winter (Figures 3d, 9a, and 10a). A marked vertical band of elevated power is evident on the velocity front that accompanied the shoreward salinity gradient (Figure 3a and 3d). When averaged over the inshore area, including this band, the spectral slope was significantly greater than zero,

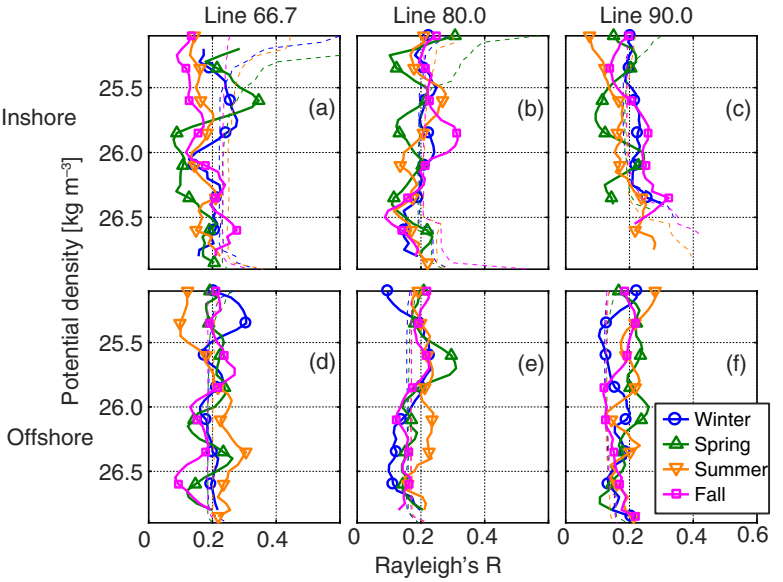

Figure 12. Vertical profiles of means of unit vectors (Rayleigh R; thick lines with symbol) constructed from the phase differences between the lower submesoscale (12–20 km) and upper submesoscale (20–30 km) spectra. Thin lines are the upper 5% bound of the confidence interval.

not only over the mesoscale to submesoscale range (12–60 km), but also at the submesoscale (12–30 km). We assume that this finer salinity structure than seen in other areas is related to the especially vigorous interaction between the equatorward CC and the poleward CUC in winter along line 66.7. The equatorward CC transporting low salinity water is intensified off Monterey Bay in winter, while the poleward CUC with its saline water also develops [*Rudnick et al*., 2017], which, in consequence, forms a most sharply defined salinity front and streaks. As the spectral slope of the inshore winter upper layer along line 66.7, including the above vertical band, is significantly greater than zero, the sharp front between the two currents alone does not explain the spectra. We suggest the development of the submesoscale turbulence emerged from this sharp front, possibly through the interaction with mesoscale eddies [e.g., *Capet et al*., 2008].

The enhancement of the submesoscale power and the elevation of the spectral slope were also observed in the inshore lower layer along line 90.0 (Figures 5g, 9c, and 10c). As observed in the Southern California Bight, the role of the CC in this case is negligible. We instead assumed that this occurred as a consequence of the interaction between the CUC and the ridges in the Southern California Bight. This might be analogous to the submesoscale turbulence induced by the CUC and the topographic curvature off Monterey Bay as presented in a submesoscale resolving model by *Molemaker et al*. [2015].

Whereas the understanding of the large-scale structure and the fluctuation of the CCS has been advanced through observations from various platforms as well as modeling [e.g., *Lynn and Simpson*, 1987; *Kelly et al*., 1998; *Chereskin et al*., 2000; *Di Lorenzo* 2003; *Rudnick et al*., 2017], structures at scales below the baroclinic Rossby radius in the interior and below the surface had been examined using only models [e.g., *Capet et al*., 2008; *Molemaker et al*., 2015] until data from towed vehicles [*Johnston et al*., 2011; *Klymak et al*., 2015] and underwater gliders became available [*Todd et al*., 2012; *Pelland et al*., 2013]. Using the underwater glider data from CUGN that has accumulated high-horizontal-resolution temperature and salinity profiles since 2007, we examined the spatial distribution and seasonal fluctuations of the fine-scale isopycnal salinity variability in the CCS, partly updating the results of *Todd et al*. [2012]. Seasonal enhancement of the fine-scale variability was clearly quantified for the three lines off Monterey Bay (line 66.7), Point Conception (line 80.0), and Dana Point (line 90.0). The mesoscale and submesoscale variations were typically enhanced in summer around the salinity front, and were strongest along line 66.7 and weakest along line 90.0 (Figure 3–5). We suggest that the strong submesoscale power in the upper layer is caused by the salinity gradient between the subarctic water transported by the CC and the equatorial water carried by the CUC, and in the lower layer below 26.3 kg m^{-3}, the contribution of the NPIW that has a core around 26.8 kg m^{-3} is suggested.

The spectral slopes over the mesoscale to submesoscale (12–60 km) were often significantly different from zero (31%–35% of the available data), whereas the slope values calculated over the submesoscale (12–30 km) were closer to zero (7.2%–8.6% data were significantly positive and 9.7%–16% of the data were significantly negative). The apparent inconsistency with the theoretical argument at the submesoscale that predicts the k^{+1} slope can be explained by the occurrence of sharp fronts. In some areas, where the marked confluence of the two currents occurs (such as line 66.7 in winter), or interaction between the currents and topography is expected (such as the inshore lower layer of line 90.0), submesoscale variability is enhanced and the spectral slopes deviate from zero.

As the fine-scale salinity variability is linked to the large-scale fields, the influence of recent anomalous warming that caused changes in the water properties and currents [*Zaba and Rudnick*, 2016; *Jacox et al*., 2016] was probably significant. Quantification of the changes in the fine-scale fields and relevant processes caused by this event will be presented in future studies.

Acknowledgments
We thank the California Underwater Glider Network operated and supported by the Instrument Development Group at Scripps Institution of Oceanography, including Jeff Sherman, Kyle Grindley, Ben Reineman, Evan Randall-Goodwin, and Derek Vana. This work was supported by the National Oceanic and Atmospheric Administration (NOAA) Climate Observation Division through grants NA15OAR4320071 and NA10OAR4320156, and by NOAA Integrated Ocean Observing System through grant NA16NOS012022, and by MEXT/JSPS KAKENHI grant JP26929099 and JP24121002. Data from the California Underwater Glider Network can be obtained from spraydata.ucsd.edu [*Rudnick* 2016a].

References

Bograd, S. J., M. P. Buil, E. D. Lorenzo, C. G. Castro, I. D. Schroeder, R. Goericke, C. R. Anderson, C. Benitez-Nelson, and F. A. Whitney (2015), Changes in source waters to the Southern California Bight, *Deep Sea Res., Part II*, *112*, 42–52, doi:10.1016/j.dsr2.2014.04.009.

Callies, J., and R. Ferrari (2013), Interpreting energy and tracer spectra of upper-ocean turbulence in the submesoscale range (1–200 km), *J. Phys. Oceanogr.*, *43*(11), 2456–2474, doi:10.1175/jpo-d-13-063.1.

Capet, X., J. C. McWilliams, M. J. Molemaker, and A. F. Shchepetkin (2008), Mesoscale to submesoscale transition in the California current system. Part I: Flow structure, eddy flux, and observational tests, *J. Phys. Oceanogr.*, *38*(1), 29–43, doi:10.1175/2007jpo3671.1.

Chelton, D. B., and M. G. Schlax (1996), Global observations of oceanic Rossby waves, *Science*, *272*(5259), 234–238.

Chereskin, T. K., M. Y. Morris, P. P. Niiler, P. M. Kosro, R. L. Smith, S. R. Ramp, C. A. Collins, and D. L. Musgrave (2000), Spatial and temporal characteristics of the mesoscale circulation of the California Current from eddy-resolving moored and shipboard measurements, *J. Geophys. Res.*, *105*(C1), 1245–1269, doi:10.1029/1999JC900252.

Cole, S. T., and D. L. Rudnick (2012), The spatial distribution and annual cycle of upper ocean thermohaline structure, *J. Geophys. Res.*, *117*, C02027, doi:10.1029/2011JC007033.

Cole, S. T., D. L. Rudnick, and J. A. Colosi (2010), Seasonal evolution of upper-ocean horizontal structure and the remnant mixed layer, *J. Geophys. Res.*, *115*, C04012, doi:10.1029/2009JC005654.

Collins, C. A., T. Margolina, T. A. Rago, and L. Ivanov (2013), Looping RAFOS floats in the California Current System, *Deep Sea Res., Part II*, *85*, 42–61, doi:10.1016/j.dsr2.2012.07.027.

Di Lorenzo, E. (2003), Seasonal dynamics of the surface circulation in the Southern California Current System, *Deep Sea Res., Part II*, *50*(14–16), 2371–2388, doi:10.1016/s0967-0645(03)00125-5.

Ferrari, R., and D. L. Rudnick (2000), Thermohaline variability in the upper ocean, *J. Geophys. Res.*, *105*(C7), 16,857–16,883, doi:10.1029/2000JC900057.

Fischer, N. I. (1995), *Statistical Analysis of Circular Data*, revised ed., 296 pp., Cambridge Univ. Press, Cambridge, U. K.

Garfield, N., C. A. Collins, R. G. Paquette, and E. Carter (1999), Lagrangian exploration of the California Undercurrent, 1992–95, *J. Phys. Oceanogr.*, *29*(4), 560–583, doi:10.1175/1520-0485(1999)029 < 0560:LEOTCU>2.0.CO;2.

Haney, R. L., R. A. Hale, and D. E. Dietrich (2001), Offshore propagation of eddy kinetic energy in the California Current, *J. Geophys. Res.*, *106*(C6), 11,709–11,717, doi:10.1029/2000JC000433.

Jacox, M. G., E. L. Hazen, K. D. Zaba, D. L. Rudnick, C. A. Edwards, A. M. Moore, and S. J. Bograd (2016), Impacts of the 2015–2016 El Niño on the California Current System: Early assessment and comparison to past events, *Geophys. Res. Lett.*, *43*, 7072–7080, doi:10.1002/2016GL069716.

Johnston, T. M. S., D. L. Rudnick, and E. Pallas-Sanz (2011), Elevated mixing at a front, *J. Geophys. Res.*, *116*, C11033, doi:10.1029/2011JC007192.

Kelly, K. A., R. C. Beardsley, R. Limeburner, K. H. Brink, J. D. Paduan, and T. K. Chereskin (1998), Variability of the near-surface eddy kinetic energy in the California Current based on altimetric, drifter, and moored current data, *J. Geophys. Res.*, *103*(C6), 13,067–13,083, doi:10.1029/97JC03760.

Klymak, J. M., W. Crawford, M. H. Alford, J. A. MacKinnon, and R. Pinkel (2015), Along-isopycnal variability of spice in the North Pacific, *J. Geophys. Res. Oceans*, *120*, 2287–2307, doi:10.1002/2013JC009421.

Kunze, E., J. M. Klymak, R. C. Lien, R. Ferrari, C. M. Lee, M. A. Sundermeyer, and L. Goodman (2015), Submesoscale water-mass spectra in the Sargasso Sea, *J. Phys. Oceanogr.*, *45*(5), 1325–1338, doi:10.1175/jpo-d-14-0108.1.

Lynn, R. J., and J. J. Simpson (1987), The California Current system: The seasonal variability of its physical characteristics, *J. Geophys. Res.*, *92*(C12), 12,947–12,966, doi:10.1029/JC092iC12p12947.

MacKinnon, J., et al. (2016), A tale of two spicy seas, *Oceanography*, *29*(2), 50–61, doi:10.5670/oceanog.2016.38.

Molemaker, M. J., J. C. McWilliams, and W. K. Dewar (2015), Submesoscale instability and generation of mesoscale anticyclones near a separation of the California undercurrent, *J. Phys. Oceanogr.*, *45*(3), 613–629, doi:10.1175/jpo-d-13-0225.1.

Pelland, N. A., C. C. Eriksen, and C. M. Lee (2013), Subthermocline eddies over the Washington continental slope as observed by Seagliders, 2003–09, *J. Phys. Oceanogr.*, *43*(10), 2025–2053, doi:10.1175/jpo-d-12-086.1.

Reid, J. L., and R. A. Schwartzlose (1962), Direct measurements of the Davidson Current off Central California, *J. Geophys. Res.*, *67*(6), 2491–2497.

Rudnick, D. L. (2016a), *California Underwater Glider Network*, I. D. G. Scripps Inst. of Oceanogr., La Jolla, Calif., doi:10.21238/S8SPRAY1618.

Rudnick, D. L. (2016b), Ocean research enabled by underwater gliders, *Ann. Rev. Mar. Sci.*, *8*, 519–541, doi:10.1146/annurev-marine-122414-033913.

Rudnick, D. L., and S. T. Cole (2011), On sampling the ocean using underwater gliders, *J. Geophys. Res.*, *116*, C08010, doi:10.1029/2010JC006849.

Rudnick, D. L., R. E. Davis, and J. T. Sherman (2016), Spray underwater glider operations, *J. Atmos. Oceanic Technol.*, *33*(6), 1113–1122, doi:10.1175/jtech-d-15-0252.1.

Rudnick, D. L., K. D. Zaba, R. E. Todd, and R. E. Davis (2017), A climatology of the California Current System from a network of underwater gliders, *Prog. Oceanogr.*, *154*, 64–106, doi:10.1016/j.pocean.2017.03.002.

Schönau, M. C., and D. L. Rudnick (2015), Glider observations of the North Equatorial Current in the western tropical Pacific, *J. Geophys. Res. Oceans*, *120*, 3586–3605, doi:10.1002/2014JC010595.

Scott, R. K. (2006), Local and nonlocal advection of a passive scalar, *Phys. Fluids*, *18*(11), 116601, doi:10.1063/1.2375020.

Sherman, J., R. E. Davis, W. B. Owens, and J. Valdes (2001), The autonomous underwater glider "Spray," *IEEE J. Oceanic Eng.*, *26*, 437–446.

Strub, P. T., and C. James (2000), Altimeter-derived variability of surface velocities in the California Current System: 2. Seasonal circulation and eddy statistics, *Deep Sea Res., Part II*, *47*(5–6), 831–870, doi:10.1016/s0967-0645(99)00129-0.

Talley, L. D. (1993), Distribution and formation of North Pacific intermediate water, *J. Phys. Oceanogr.*, *23*(3), 517–537.

Todd, R. E., D. L. Rudnick, M. R. Mazloff, B. D. Cornuelle, and R. E. Davis (2012), Thermohaline structure in the California Current System: Observations and modeling of spice variance, *J. Geophys. Res.*, *117*, C02008, doi:10.1029/2011JC007589.

Torrence, C., and G. P. Compo (1998), A practical guide to wavelet analysis, *Bull. Am. Meteorol. Soc.*, *79*, 61–78.

Vallis, G. K. (2006), *Atmospheric and Oceanic Fluid Dynamics: Fundamentals and Large-scale Circulation*, Cambridge Univ. Press, Cambridge.

Yasuda, I. (1997), The origin of the North Pacific intermediate water, *J. Geophys. Res.*, *102*(C1), 893–909.

Zaba, K. D., and D. L. Rudnick (2016), The 2014–2015 warming anomaly in the Southern California Current System observed by underwater gliders, *Geophys. Res. Lett.*, *43*, 1241–1248, doi:10.1002/2015GL067550.